

1 CD47 prevents Rac-mediated phagocytosis 2 through Vav1 dephosphorylation

3

4 Wyatt D Miller¹, Abhinava K Mishra², Connor J Sheedy¹, Annalise Bond², Brooke M
5 Gardner², Denise J Montell², Meghan A Morrissey^{2*}

6

7 ¹ Interdisciplinary Program in Quantitative Biology, University of California, Santa
8 Barbara, Santa Barbara CA

9 ² Molecular Cellular and Developmental Biology Department, University of California,
10 Santa Barbara, Santa Barbara CA

11

12 ³ Lead contact

13 [*morrissey@ucsb.edu](mailto:morrissey@ucsb.edu)

14

15 Keywords: macrophage, phagocytosis, Fc Receptor, IgG, CD47, SIRP α

16 **Summary**

17 CD47 is expressed by viable cells to protect against phagocytosis. CD47 is recognized
18 by SIRP α , an inhibitory receptor expressed by macrophages and other myeloid cells.
19 Activated SIRP α recruits SHP-1 and SHP-2 phosphatases but the inhibitory signaling
20 cascade downstream of these phosphatases is not clear. In this study, we used time
21 lapse imaging to measure how CD47 impacts the kinetics of phagocytosis. We found
22 that targets with IgG antibodies were primarily phagocytosed through a Rac-based
23 reaching mechanism. Targets also containing CD47 were only phagocytosed through a
24 less frequent Rho-based sinking mechanism. Hyperactivating Rac2 eliminated the
25 suppressive effect of CD47, suggesting that CD47 prevents activation of Rac and
26 reaching phagocytosis. During IgG-mediated phagocytosis, the tyrosine kinase Syk
27 phosphorylates the GEF Vav, which then activates the GTPase Rac to drive F-actin
28 rearrangement and target internalization. CD47 inhibited Vav1 phosphorylation without
29 impacting Vav1 recruitment to the phagocytic synapse or Syk phosphorylation.
30 Macrophages expressing a hyperactive Vav1 were no longer sensitive to CD47.
31 Together this data suggests that Vav1 is a key target of the CD47 signaling pathway.

32 Introduction

33 The immune system is regulated by a combination of activating signals on
34 pathogenic targets and inhibitory signals that protect healthy tissue¹. Inhibitory immune
35 receptors are critical for tolerance in healthy tissues, and restoring homeostasis after
36 injury and infection²⁻⁴. Macrophages, effectors of the innate immune system, protect the
37 body by phagocytosing harmful targets while robustly ignoring healthy cells. CD47 is an
38 inhibitory signal on the surface of viable cells that prevents phagocytosis^{5,6}. Compared
39 to their activating counterparts, the inhibitory signals that protect healthy cells remain
40 poorly understood.

41 IgG antibodies bind bacteria, fungi or virally infected cells and trigger
42 phagocytosis^{5,7,8}. Antibody dependent phagocytosis is also an important mechanism for
43 many cancer immunotherapies including rituximab (CD20 antibody) and trastuzumab
44 (Her2 antibody)⁹⁻¹². IgG is recognized by the Fc Receptor in macrophages¹³. IgG
45 binding triggers Fc Receptor phosphorylation and recruits the effector kinase Syk. Syk
46 activates several downstream pathways to promote F-actin reorganization and
47 phagocytosis.

48 To avoid phagocytosis of healthy cells, CD47 is a potent “Don’t Eat Me” signal
49 expressed by nearly all viable cells in mice and humans¹⁴⁻¹⁶. CD47 suppresses
50 phagocytosis by activating the inhibitory receptor SIRP α in macrophages¹⁷⁻²¹. Cells
51 lacking CD47 are rapidly cleared from healthy tissues^{14,16}. Bacteria mimic CD47 to
52 evade the innate immune system²²⁻²⁴. CD47 is also upregulated on many cancer cells,
53 allowing these malignant cells to evade the immune system and proliferate
54 unchecked^{14,15,25}.

55 Modulating the CD47 signaling pathway has broad therapeutic implications. In
56 cancer treatment, CD47 blockades have shown promising results in several phase I and
57 phase II clinical trials, often administered in combination with a therapeutic IgG antibody
58 that activates phagocytosis of cancer cells^{6,26–30}. CD47 blockades promote both
59 phagocytosis of cancer cells by macrophages and cross-presentation of cancer antigen
60 by dendritic cells^{15,31,32}. CD47 blockades also improve phagocytosis of diseased
61 vascular tissue to treat atherosclerosis and clearance of viral infections^{33,34}. Conversely,
62 activating the CD47 signaling pathway has many potential therapeutic applications.
63 Adding CD47 to transplanted cells or materials is an exciting strategy to protect these
64 materials from macrophage phagocytosis^{35–38}. Similarly, activating the CD47 receptor,
65 SIRP α , is a potential therapy for auto-immune disorders to counteract macrophage
66 hyperactivation^{39,40}.

67 Despite the immense therapeutic interest in CD47 and its receptor SIRP α , very
68 little is known about how this inhibitory signal is transduced within the macrophage.
69 CD47 binding positions SIRP α at the phagocytic synapse between a macrophage and
70 its target, where SIRP α 's two intracellular immune tyrosine inhibitory motifs (ITIMs) are
71 phosphorylated by Src family kinases^{41,42}. The phosphorylated ITIM motifs recruit SHP-
72 1 and SHP-2 phosphatase, and SHP-1 is required for CD47 to inhibit phagocytosis^{17–}
73 ^{19,43–45}. The substrates of these phosphatases during phagocytosis have not been
74 identified. Several studies have shown that SHP-1/2 phosphatases do not directly de-
75 activate the IgG-binding Fc Receptor^{17,42,46}. Downstream, this inhibitory signaling
76 pathway prevents activation of integrin and myosin II^{42,46}. However, there are many

77 signaling events between Fc Receptor phosphorylation and the inside out activation of
78 integrins or myosin II, leaving several potential targets for SIRP α -bound phosphatases⁵.

79 In this study, we clarified the downstream signaling cascade enacted by CD47,
80 and determined how this inhibitory pathway affects phagocytosis of antibody-bound
81 targets. We used timelapse microscopy to characterize how CD47 affected each step in
82 the phagocytic process. For IgG opsonized targets, we observed two previously
83 described modes of phagocytosis regulated by different GTPases. Most targets were
84 phagocytosed via Rac-driven reaching phagocytosis and a smaller number through Rho-
85 driven sinking phagocytosis. Targets with CD47 were only phagocytosed through the
86 less frequent Rho-based sinking mechanism. Inhibiting Rho eliminated phagocytosis of
87 synthetic targets and cancer cells with CD47, while inhibiting Rac had little effect. A
88 hyperactive Rac2 mutation (Rac2^{E62K}) bypassed CD47's inhibitory effect. This
89 demonstrates that CD47 inhibits Rac-driven reaching phagocytosis, and suggests that
90 the direct targets of SIRP α -bound phosphatases are upstream of Rac. We found CD47
91 causes dephosphorylation of Vav1, the guanine nucleotide exchange factor (GEF) that
92 activates Rac but not Rho at the phagocytic cup. CD47 did not cause any change in Syk
93 activation or Vav1 recruitment, suggesting that Vav1 is directly regulated by SHP
94 phosphatases. Overall, our study provides a mechanistic model for how CD47
95 suppresses phagocytosis.

96 **Results**

97 **CD47 slows phagocytosis and increases cup retraction and failure**

98 To study how CD47 inhibits IgG-mediated phagocytosis, we used reconstituted,
99 cell-mimicking engulfment targets consisting of silica beads coated with fluorescent
100 supported lipid bilayers (Fig. 1A, 1B)^{42,47}. To activate Fc Receptor-mediated
101 phagocytosis, we opsonized beads with anti-biotin IgG, which binds biotinylated lipids in
102 the bilayers. We incorporated His-tagged CD47 onto beads via attachment to Ni-NTA-
103 conjugated lipids, so that the CD47 extracellular domain is positioned to activate SIRP α .
104 We then incubated primary mouse bone marrow-derived macrophages (BMDMs) with
105 IgG or IgG+CD47 beads and measured the number of internalized beads via confocal
106 microscopy (Fig. 1A, 1B). IgG beads were engulfed approximately two times more than
107 IgG+CD47 beads (Fig. 1B), consistent with previous studies^{42,48}.

108 We next used time-lapse confocal microscopy to determine how CD47 affects
109 the kinetics of phagocytosis. Phagocytosis consists of discrete steps, each associated
110 with unique molecular mediators: (1) target particle binding, (2) initiation of
111 phagocytosis, and (3) completion, as defined by phagocytic cup closure (Fig. 1C, D).
112 We measured the frequency of completing each step for IgG and IgG+CD47 beads. We
113 also measured the time between successfully completing each step (Fig. 1E-I). We
114 found that CD47 did not inhibit target binding (Fig. 1E). We also found no difference in
115 the frequency of initiating phagocytosis or the time between bead binding and initiation
116 of phagocytosis (Fig. 1F, 1G). However, CD47 decreased the frequency of successfully
117 completing phagocytosis (Fig. 1I). Most strikingly, CD47 dramatically slowed the
118 engulfment time, or the time between initiation and completion of phagocytosis (Fig.

119 1H). These results indicate that CD47 affects the progression of macrophage
120 membrane around the phagocytic target or phagocytic cup closure, rather than target
121 particle binding or initiation of phagocytosis.

122 **CD47 positive targets are phagocytosed via sinking phagocytosis**

123 Since the engulfment speed of IgG and IgG+CD47 targets was dramatically
124 different, we hypothesized that engulfment of the two bead types may be
125 morphologically distinct. In our timelapse data, we clearly observed two previously
126 described forms of phagocytosis: reaching and sinking phagocytosis⁴⁹⁻⁵². Reaching
127 phagocytosis involves rapid extension of F-actin rich protrusions around the phagocytic
128 target^{49,52-54}. During sinking phagocytosis, the target is slowly pulled into the cell without
129 membrane extension^{49,50,52,55}. We found that IgG beads were almost always engulfed
130 via reaching phagocytosis (Fig. 2A, C, Video S1), whereas IgG+CD47 beads were
131 usually engulfed via sinking phagocytosis (Fig. 2B, C, Video S2). This is consistent with
132 the slower engulfment speed of IgG+CD47 targets. To quantify the frequency of these
133 two modes of phagocytosis more rigorously, we measured the position of the
134 engulfment target relative to the cell cortex when phagocytosis was completed (Fig.
135 2D)⁵⁵. This analysis revealed two populations of engulfed targets: one located outside
136 the cell cortex at the time of cup closure (beads engulfed via reaching phagocytosis),
137 and one located inside the cell cortex (beads engulfed via sinking phagocytosis). For
138 IgG beads, 80% were outside the cell when phagocytosis completed. In contrast, the
139 majority of IgG+CD47 targets were inside the cell when the phagocytic cup closed.

140 We found that the increased failure rate of phagocytosis of CD47 targets was
141 due to increased retraction of reaching phagocytic cups. If the macrophage initiated

142 reaching phagocytosis of a target with CD47, the phagocytic cup usually retracted
143 before it extended around the entire target, resulting in failed reaching phagocytosis
144 (Fig. 2E, F; Video S3). In contrast, retraction of reaching phagocytic cups was rarely
145 observed for IgG-only targets (Fig. 2E). Together these data indicate that CD47 inhibits
146 reaching phagocytosis, but not sinking phagocytosis.

147 **Rho, not Rac, is required for phagocytosis of CD47 positive targets**

148 Reaching and sinking phagocytosis are characterized by distinct actin
149 cytoskeleton dynamics^{52,55}. One measurable difference is that F-actin accumulates at
150 the phagocytic cup rim during reaching but not sinking phagocytosis⁵⁵. To test if CD47
151 changes F-actin organization at the phagocytic cup, we incubated BMDMs with IgG and
152 IgG+CD47 beads, then fixed and stained with phalloidin to visualize F-actin during
153 phagocytosis (Fig. 3A, B). Actin recruitment to phagocytic cup rims was significantly
154 reduced during engulfment of IgG+CD47 targets compared to IgG targets (Fig. 3B). This
155 suggests that CD47 alters actin organization during phagocytosis.

156 The Rho GTPase family (Rac, Rho and Cdc42) are regulators of the actin
157 cytoskeleton during phagocytosis, and different GTPases have been implicated in
158 reaching and sinking phagocytosis. Reaching phagocytosis is regulated by the GTPase
159 Rac while sinking phagocytosis requires the GTPase Rho⁵². Since CD47 inhibits
160 reaching phagocytosis, we hypothesized that CD47 specifically inhibits Rac, but not
161 Rho. Additionally, since IgG+CD47 targets are engulfed via sinking phagocytosis, we
162 hypothesized that Rho is required for phagocytosis of IgG+CD47 target particles. To
163 test these hypotheses, we treated BMDMs with inhibitors of Rac (NSC23766 and MBQ-
164 167; also inhibit the related GTPase CDC42) or an inhibitor of Rho (C3 transferase). We

165 then incubated the BMDMs with IgG, IgG+CD47, or unopsonized beads (Fig. 3C). Rac
166 inhibition significantly reduced phagocytosis of IgG targets, causing BMDMs to eat the
167 same amount of IgG and IgG+CD47 beads. Rac inhibition did not affect phagocytosis of
168 IgG+CD47 targets. On the other hand, Rho inhibition decreased phagocytosis of both
169 target types, nearly eliminating phagocytosis of IgG+CD47 targets. Together, this data
170 supports the hypothesis that CD47 inhibits Rac-mediated phagocytosis. This data also
171 demonstrates that Rho, not Rac, is required for phagocytosis of IgG+CD47 targets.

172 We next sought to validate these results with cancer cell targets in lieu of
173 synthetic bead targets. We hypothesized that CD47-expressing cancer cells, like
174 IgG+CD47 beads, are phagocytosed through a Rho-dependent mechanism, while CD47
175 knockout cells, like IgG beads, are primarily phagocytosed via Rac and Cdc42. To test
176 this, we measured phagocytosis of L1210 mouse leukemia cells opsonized with an anti-
177 CD20 antibody. This is modeled after the clinical combination of CD20 antibodies and
178 CD47 blockade, which has shown promise in clinical trials²⁷. We used CRISPR-Cas9 to
179 generate a monoclonal CD47^{KO} L1210 line (Supp Fig. 3). We confirmed that CD47 was
180 not expressed on these cells by staining for CD47 (Supp Fig. 3). We again treated
181 BMDMs with pharmacological inhibitors of Rac or Rho, then incubated them with the
182 opsonized WT or CD47^{KO} L1210s and monitored phagocytosis via live cell microscopy
183 (Fig. 3D). As expected, untreated BMDMs engulfed more CD47^{KO} L1210 cells than WT
184 L1210 cells. Pharmacological inhibition of Rac decreased phagocytosis of CD47^{KO}
185 L1210 cells, but did not affect phagocytosis of wild type L1210 cells. In contrast, Rho
186 inhibition decreased engulfment of both CD47^{KO} and wild type L1210 cells, completely

187 eliminating phagocytosis of wild type cells. Together, this demonstrates that CD47
188 inhibits Rac-mediated phagocytosis of antibody opsonized cancer cells.

189 **Hyperactive Rac2 overcomes CD47 inhibition**

190 Our results show that inhibiting Rac mirrors the effect of CD47, however the
191 direct targets of SIRP α -bound phosphatases could be upstream or downstream of Rac.
192 We next hypothesized that if the direct targets are upstream of Rac, then
193 hyperactivating Rac could overcome CD47-mediated inhibition of phagocytosis. In
194 contrast, if CD47 inhibits later steps in phagocytosis, hyperactivating Rac could promote
195 phagocytosis but targets with CD47 would still be engulfed less than cells without CD47.
196 To test this, we isolated BMDMs from mice heterozygous for the hyperactive Rac2^{E62K}
197 mutation (Rac2^{E62K/+})^{56,57}. This Rac2 mutation is associated with a moderate increase in
198 Rac activity⁵⁶. We found that Rac2^{E62K/+} and wildtype macrophages phagocytosed a
199 similar amount of antibody-opsonized CD47^{KO} L1210 cells. However, Rac2^{E62K/+}
200 macrophages were insensitive to CD47 and phagocytosed dramatically more wild type
201 L1210 cells compared to wild type macrophages (Fig. 4A-E; Video S4). This data
202 demonstrates that increasing Rac activity bypasses the inhibitory effect of CD47.

203 **CD47 inhibits Rac through dephosphorylation of Vav1**

204 We next considered the potential direct targets of SIRP α -bound phosphatases.
205 We did not expect SIRP α -bound phosphatases to directly target Rac, as Rac GTPases
206 are primarily regulated by GTP-binding and hydrolysis, rather than phosphorylation.
207 Instead, we hypothesized that the direct target of SIRP α -bound phosphatases is
208 upstream of Rac. Since CD47 does not inhibit Rho-mediated phagocytosis, we

209 reasoned that the early steps in phagocytosis, required for both sinking and reaching
210 phagocytosis, are also unlikely to be the direct target of SIRP α -bound phosphatases.
211 After IgG binds the Fc Receptor, IgG and Fc Receptor form nanoscale clusters within
212 the plasma membrane^{58–60}. At these clusters, the Fc Receptor intracellular ITAMs are
213 phosphorylated and recruit Syk kinase^{59–61}. We have previously found that CD47 does
214 not affect Fc Receptor clustering or alter Syk recruitment to these clusters⁴². In addition,
215 other studies have found little or no change in Fc Receptor or Syk phosphorylation for
216 CD47-positive targets^{17,46}. To confirm this, we incubated macrophages with
217 unopsonized, IgG, or IgG+CD47 beads, and measured Syk phosphorylation (pY346) by
218 western blot. As expected, IgG beads increased Syk phosphorylation, and the addition
219 of CD47 to IgG beads did not reduce the IgG-mediated Syk phosphorylation (Fig. 5A,
220 B). Taken together, these data suggest that the direct target of SIRP α -bound
221 phosphatases is downstream of Syk but upstream of Rac.

222 As a GTPase, Rac activation is regulated by Guanine nucleotide Exchange
223 Factors (GEFs) that promote the exchange of GDP for GTP. Vav1 is the GEF that
224 activates Rac during phagocytosis^{62,63}. Vav1 is an attractive potential target for SIRP α -
225 bound phosphatases for several reasons. First, Vav1 is required for Rac, but not Rho,
226 activity during phagocytosis⁶⁴. Second, Syk phosphorylates Vav1 on tyrosine Y174 to
227 activate Vav1, making Vav1 the direct link between Syk and Rac⁶⁵. Finally, in NK cells,
228 SHP-1 directly dephosphorylates Vav1 to prevent target cell killing, suggesting that this
229 SIRP α -bound phosphatase can directly regulate Vav1^{66,67}. Supporting this, the
230 sequence surrounding the Y174 site on Vav1 (DEIpYEDL) closely matches the optimal
231 SHP-1 target sequences from two previous studies ((D/E)X(L/I/V)XpYXX(L/I/V) and

232 (D/EXpY)) in both mouse and humans^{68,69}. We hypothesized that SIRP α -bound
233 phosphatases could target Vav1 to inhibit phagocytosis. We first assayed Vav1
234 phosphorylation using a phosphoVav1 antibody (pY174)^{70,71}. We found that
235 macrophages incubated with IgG beads showed increased Vav1 phosphorylation, and
236 adding CD47 to the beads eliminated this increase (Fig. 5A, C). To confirm the phospho
237 antibody staining, we immunoprecipitated Vav1 and used a pan-phosphotyrosine
238 antibody to measure Vav1 phosphorylation (Fig. 5D, E). This confirmed that IgG
239 increased Vav1 phosphorylation, and CD47 eliminated this increase. This data shows
240 that CD47 eliminates IgG-induced Vav1 phosphorylation.

241 **CD47 does not prevent Vav1 recruitment to the phagocytic synapse**

242 We next sought to clarify the mechanism by which CD47 reduces Vav1
243 phosphorylation. We began by examining Vav1 localization in the phagocytic synapse
244 using TIRF microscopy. Vav1 binds directly to Syk, but may have other binding partners
245 at the phagocytic cup^{65,72}. In particular, Rac, which directly binds to Vav, is active
246 throughout the actin-rich extensions that surround the phagocytic target⁷³⁻⁷⁵. We
247 constructed planar supported lipid bilayers on a glass coverslip, then imaged IgG
248 clustering and mCherry-Vav1. We found that on IgG bilayers, Vav1 was enriched at IgG
249 clusters, but also present throughout the phagocytic synapse (Fig. 6A). This is
250 consistent with the reported interaction of Vav1 with Syk, present at IgG clusters, and
251 Rac, present along the sides of the phagocytic cup^{59,73}.

252 SIRP α -bound phosphatases could reduce Vav1 phosphorylation either by
253 preventing recruitment to IgG clusters where Vav1 is phosphorylated, or by
254 dephosphorylating Vav1 directly. To distinguish between these possibilities, we used

255 TIRF imaging to measure Vav1 recruitment to a phagocytic synapse containing CD47.
256 We verified that CD47 inhibited cell spreading across the bilayer, demonstrating that the
257 CD47 pathway was active (Fig. 6C). IgG cluster size was not affected by CD47,
258 consistent with previous literature (Fig. 6A, B)⁴². CD47 did not reduce Vav1 recruitment
259 to IgG clusters (Fig. 6A, B). In fact, Vav1 localization correlated even more strongly with
260 IgG when CD47 was present (Fig. 6D). Since the Vav1 signal at IgG clusters is similar
261 with IgG or IgG+CD47, this increased colocalization is likely due to a decrease in Vav1
262 outside of the IgG clusters. Overall, this demonstrates that CD47 does not prevent Vav1
263 recruitment to IgG clusters.

264 **Hyperactive Vav1 eliminates the effect of CD47**

265 Since our data suggests that SHP-1 directly dephosphorylates Vav, we
266 hypothesized that constitutive Vav1 activity would be sufficient to bypass the
267 suppressive effect of CD47. Phosphorylation of Y174 on Vav1 displaces this residue
268 from its intramolecular binding pocket, relieving autoinhibition of Vav1⁷⁶. Similarly,
269 mutating this residue to phenylalanine results in a constitutively active Vav1⁷⁷. We used
270 a previously characterized hyperactive Vav1 construct, where Y174 and two other key
271 tyrosines (Y142 and Y160) are mutated to prevent Vav1 autoinhibition^{77,78}.
272 Macrophages expressing this mutant Vav1 were not sensitive to CD47, phagocytosing a
273 comparable amount of IgG or IgG+CD47 beads (Fig. 6E). Together, this data strongly
274 suggests that Vav1 dephosphorylation is critical for CD47 to inhibit phagocytosis.

275 Discussion

276 CD47 is a potent “Don’t Eat Me” signal that protects healthy cells and cancer
277 cells from macrophage attack. Understanding how CD47 inhibits phagocytosis of
278 antibody-bound targets is particularly important, since combining CD47 blockades and
279 monoclonal antibody therapies is the subject of several ongoing clinical trials^{6,27–29}. We
280 examined the inhibitory signaling cascade enacted by CD47. We show that CD47
281 specifically inhibits Rac-mediated reaching phagocytosis, but not Rho-mediated sinking
282 phagocytosis. We consider each step in the phagocytosis signaling cascade leading to
283 Rac activation, and demonstrate that Vav1 is the key target of SIRP α -bound
284 phosphatases (Fig. 6F).

285 We show that Vav1 is dephosphorylated in response to CD47, and that
286 constitutively active Vav1 rescues phagocytosis of CD47-positive targets (Fig. 6). This
287 demonstrates that Vav1 is a key target of the CD47 signaling cascade. There are
288 several reasons to think that Vav1 is directly dephosphorylated by SIRP α -bound
289 phosphatases SHP-1 and SHP-2. After Fc Receptor activation, Syk binds to the Fc
290 Receptor’s phosphorylated ITAMs. Vav1 binds to Syk, and is activated by Syk
291 phosphorylation^{65,72}. When CD47 is present, we find no difference in IgG cluster size,
292 Syk recruitment or Syk phosphorylation, consistent with previous literature^{17,42,46}. This
293 suggests that the phagocytosis signaling cascade upstream of Vav1 is not affected by
294 CD47. We further demonstrate that CD47 does not affect Vav1 recruitment to IgG
295 clusters, arguing against an indirect effect on Vav1 due to upstream changes in
296 signaling preventing Vav1 recruitment to the phagocytic synapse. In addition, Vav1 is
297 directly dephosphorylated by SHP-1 in NK cells^{66,67}. SHP-1 also dephosphorylates Vav1

298 to prevent Fas internalization and cell death in B cells⁷⁹. We propose SHP-1 can also
299 dephosphorylate Vav1 at the phagocytic synapse.

300 Our findings explain a number of results in the current literature, which could be
301 downstream consequences of Vav1 inactivation. First, we have previously shown that
302 CD47 prevents inside out activation of integrin⁴². Vav family GEFs are required for
303 integrin activation during many immune cell processes including phagocytosis, cell
304 migration and cell spreading^{80–83,83–85}. Another study found that CD47 prevents myosin
305 II phosphorylation, which is often required for phagocytosis⁴⁶. This could be a
306 downstream effect of Rac inhibition, since Rac promotes myosin II activation, or
307 because myosin II is required for later steps in the phagocytosis program than Rac^{86,87}.
308 While it is possible that SIRP α -bound phosphatases target multiple proteins at the
309 phagocytic synapse including both myosin II and Vav1, our finding that Vav1 activation
310 rescues phagocytosis of CD47-positive targets supports the idea that Vav1 is the
311 primary target of SIRP α -bound phosphatases.

312 Our work also provides some insight into Vav1 function during phagocytosis.
313 There are very compelling studies showing that Vav1 binds directly to Syk via its SH2
314 domain, and this interaction promotes Vav1 phosphorylation both with purified proteins
315 and in cells^{65,72}. Vav1 phosphorylation relieves Vav1 autoinhibition⁷⁶. Once
316 phosphorylated via this transient interaction, Vav1 remains in the active conformation
317 until dephosphorylated⁷². During phagocytosis, we envision that Vav1 is activated by
318 Syk at IgG clusters, but moves on to activate Rac at other locations in the phagocytic
319 cup. Rac is active along the sides and base of the phagocytic cup⁷³. Vav1 may be
320 targeted by SIRP α -bound phosphatases after leaving IgG clusters, since we have

321 previously seen that SIRP α does not colocalize with IgG clusters⁴². This would explain
322 our TIRF data showing a reduction in Vav1 at the phagocytic synapse outside of IgG
323 clusters when CD47 is also present.

324 One question raised by our study is whether the mechanism of phagocytosis
325 (reaching vs sinking phagocytosis) affects phagosome processing. Other studies have
326 suggested that the mode of target entry can affect what proteins are recruited to the
327 phagosome^{52,88,89}. Rac and Vav1 also have known roles in phagosome processing⁶⁴.
328 Interestingly, CD47 blockades enhance cross presentation, which could be due to a
329 change in phagocytosis by dendritic cells, a change in the subsequent processing of the
330 phagocytosed material to promote cross presentation, or a separate signaling pathway
331 in dendritic cells^{32,90,91}.

332 Our work has broader implications for understanding inhibitory immune
333 receptors. In macrophages, there are several other inhibitory immune receptors that
334 regulate phagocytosis⁹²⁻⁹⁶. Future studies will need to examine whether these function
335 through a shared mechanism, or whether each inhibitory signaling pathway has unique
336 targets. An interesting implication of our work is that CD47 inhibits some, but not all,
337 parts of the Fc Receptor signaling pathway. Inhibitory receptors like SIRP α are often
338 described as the counterbalance to activating receptors like the Fc Receptors. This
339 gives the impression of a single dial that can be turned up or turned down. Instead, we
340 see that CD47 strongly inhibits Rac, but has no effect on Rho. This suggests a
341 potentially more complicated situation where inhibitory receptors target specific
342 downstream signals to sculpt the macrophage response.

343 Our work has several therapeutic implications. Our finding that CD47 does not
344 inhibit Rho-mediated phagocytosis suggests that inhibitors of Rho-mediated
345 phagocytosis would synergize with CD47. In the cases where CD47 is currently used to
346 protect transplanted cells or particles, a secondary signal that inhibits Rho could be very
347 potent. This also suggests that CD47 would be more protective for targets that are
348 phagocytosed via a Rac-based mechanism than targets that are phagocytosed via a
349 Rho-based mechanism. Cancer cells can express a variety of different “Eat Me” signals,
350 and the phagocytic receptors that regulate engulfment can vary for different cancer
351 populations⁵. Our work suggests that cancer cell CD47 could potentially regulate
352 phagocytosis if the signals on the cancer cell activate Rac. Finally, this work also
353 suggests that macrophages with hyperactive Rac are insensitive to CD47, and adept at
354 phagocytosing cancer cells⁵⁷.
355

356 **Figure legends**

357

358 **Figure 1: CD47 decreases the probability of completing engulfment and slows the**

359 **engulfment process.** (A) Schematic depicts the supported lipid bilayer system used to

360 study phagocytosis. Silica beads are coated with a supported lipid bilayer containing

361 fluorescent atto647 lipids. Anti-biotin IgG binds to biotinylated lipids in the bilayer.

362 10xHis-tagged CD47 extracellular domain is attached to beads via a Ni²⁺-chelating

363 DGS-NTA lipid, so that the SIRP α binding domain is positioned outwards. (B) Beads

364 (magenta) conjugated with IgG or IgG+CD47 were incubated with mouse bone marrow

365 derived macrophages (BMDMs) expressing membrane tethered GFP (GFP-CAAX;

366 green) for 30 minutes then imaged with confocal microscopy. The average number of

367 beads engulfed per macrophage was counted and normalized to the maximum average

368 number of beads engulfed per macrophage for that experiment to control for batch to

369 batch variability in macrophage appetite. (C) Schematic depicts the stages of

370 phagocytosis: target particle binding, initiation of phagocytosis, and completion

371 (phagocytic cup closure). (D) Representative images of each stage. BMDMs are

372 expressing GFP-CAAX (green, top; greyscale, bottom) and the bead supported lipid

373 bilayer is labeled with atto647 (magenta, top). Box in the top panel shows area of inset

374 below. Timelapse confocal microscopy was used to quantify the fraction of beads bound

375 to a macrophage (E); the time from binding to initiation of phagocytosis, if it occurred

376 (F); the fraction of bound beads that proceed to the initiation step (G); the engulfment

377 time, which is the time from initiation to completion, if it completed (H); and the fraction

378 of beads that proceeded from the initiation to completion (I). For (F) and (H), the large

379 filled data points represent the mean of an independent replicate, while the smaller
380 unfilled data points of the same shape indicate individual cells quantified on the same
381 day for that replicate. For (B) each dot represents an independent replicate composed
382 of at least 100 macrophages per condition; data was compared using an unpaired t test.
383 For (E)-(I) each independent replicate composed of at least 15 engulfment events. The
384 means from four independent replicates were compared using an unpaired t test. In all
385 graphs, bars denote the mean \pm SEM. * denotes $p < 0.05$, ** denotes $p < 0.005$, ***
386 denotes $p < 0.0005$. Scale bars are $10\mu\text{m}$.

387

388 **Figure 2: CD47 shifts primary mode of phagocytosis from reaching to sinking.** (A)

389 Timelapse images show reaching phagocytosis of an IgG bead target by a BMDM.
390 White arrowheads point to extension of phagocyte membrane (GFP-CAAX, green) out
391 around the target (atto647 lipid; magenta). White arrow denotes subsequent closure of
392 the phagocytic cup while the bead remains outside the phagocyte cortex. Images
393 correspond to Video S1 (B) Timelapse images show sinking phagocytosis of IgG+CD47
394 bead. Yellow arrows show closure of the phagocytic cup when the bead is within the
395 macrophage. Images correspond to Video S2. (C) Graph depicts the fraction of
396 successful phagocytosis that occurred via sinking phagocytosis based on the apparent
397 morphology in timelapse confocal microscopy data. (D) Graph depicts the position of
398 the bead centroid relative to the phagocyte cortex when phagocytosis was completed.
399 (E) Graph depicts the fraction of retracted reaching cups out of the total number of
400 initiated reaching cups. Retracted cups were defined as cases in our timelapse data set
401 where membrane extensions grew around the target but were subsequently

402 disassembled. (F) Images show an example of failed reaching phagocytosis of an
403 IgG+CD47 bead. White arrowheads highlight extension of the macrophage membrane,
404 which is subsequently retracted. Images correspond to Video S3. For (C) and (E), the
405 averages from four independent experiments were plotted and compared using an
406 unpaired t test. Bars represent the mean \pm SEM. For (D), each data point represents an
407 individual bead ($n=60$ targets per condition from 4 independent experiments), and data
408 was compared using an unpaired t test. ** denotes $p<0.005$, *** denotes $p<0.0005$.
409 Scale bars are 10 μ m.

410

411 **Figure 3: CD47 targets distinct actin regulators.** (A, B) BMDMs were incubated with
412 IgG or IgG+CD47 beads then fixed and stained with 488 phalloidin (greyscale) to
413 visualize F-actin during phagocytosis. Enrichment of F-actin at late-stage (>50%
414 completed) phagocytic cup rims was measured by comparing the mean fluorescent
415 intensity (MFI) of phalloidin at the cup rim (red dot) to the MFI of phalloidin at the cell
416 cortex (blue line). Bead position is indicated with a dashed yellow line. (B) Graph
417 depicts data quantification described in (A). The large filled data points represent the
418 mean of an independent replicate, while the smaller unfilled data points of the same
419 shape indicate individual cells collected on that day for that replicate. Dashed line at 1
420 corresponds to no F-actin enrichment at cup rims. (C) BMDMs were treated with
421 pharmacological inhibitors of Rac and Cdc42 (NSC23766 and MBQ-167) or Rho (C3
422 transferase) for 24 hours, then incubated with IgG, IgG+CD47, or unopsonized
423 supported lipid bilayer coated beads. Phagocytosis was measured by confocal
424 microscopy. The average number of beads phagocytosed was normalized to the

425 maximum phagocytosis in that replicate. (D) BMDMs were treated with pharmacological
426 inhibitors of Rac and Cdc42 (NSC23766 and MBQ-167) or Rho (C3 transferase) for 24
427 hours, then the inhibitors were removed and replaced with fresh media. WT or CD47^{KO}
428 mouse L1210 leukemia cells were dyed with CellTrace Far Red then opsonized with an
429 anti-murine CD20 monoclonal antibody and added to the BMDMs. Phagocytosis was
430 monitored for 10 hours via timelapse microscopy. The percent of BMDMs that engulfed
431 was quantified, and data was normalized to maximum for that experiment. For (B), the
432 means of 4 independent experiments were compared using an unpaired t test. For (C)
433 and (D), each data point represents an independent experiment including quantification
434 of at least 100 macrophages. Data was compared using one-way ANOVA with Holm
435 Sidak multiple comparison test. In all graphs, bars represent the mean \pm SEM. *
436 denotes $p < 0.05$, ** denotes $p < 0.005$, *** denotes $p < 0.0005$, **** denotes $p < 0.00005$.
437 Scale bars are 10 μ m.

438

439 **Figure 4: Hyperactive Rac bypasses CD47.** (A-E) WT or CD47^{KO} mouse L1210
440 leukemia cells were dyed with CellTrace Far Red (magenta) then opsonized with an
441 anti-murine CD20 monoclonal antibody and added to the BMDMs (green) from WT or
442 Rac2^{E62K/+} mice. (A) Stills from a representative timelapse showing WT BMDMs
443 incubated with CD47^{KO} L1210 cells. Yellow arrow indicates phagocytosis. (B) Stills from
444 a representative timelapse showing Rac2^{E62K/+} BMDMs incubated with CD47^{KO} L1210
445 cells. Yellow arrow indicates phagocytosis. (C) Stills from a representative timelapse
446 showing WT BMDMs incubated with CD47-positive WT L1210 cells. (D) Stills from a
447 representative timelapse showing Rac2^{E62K/+} BMDMs incubated with CD47-positive WT

448 L1210 cells. Yellow arrow indicates phagocytosis. (E) Graphs show the phagocytosis of
449 L1210 cells during a 10 hour timelapse, normalized to the maximum phagocytosis on
450 each day. Data compared using one-way ANOVA with Holm Sidak multiple comparison
451 test. Line and bars denote mean and SEM. * denotes $p < 0.05$, ** denotes $p < 0.005$, ***
452 denotes $p < 0.0005$. Scale bars are $10\mu\text{m}$.

453

454 **Figure 5: CD47 inhibits IgG-mediated phosphorylation of Vav.** (A) BMDMs were
455 incubated with unopsonized (--), IgG, or IgG+CD47 beads for 10 minutes, then lysed
456 directly in 2X Laemmli sample buffer. Whole cell lysates were immunoblotted with the
457 indicated antibodies. Representative of $n = 3$ independent replicates. (B, C) The ratio of
458 phosphorylated Syk to total Syk or phosphorylated Vav1 to total Vav1 was quantified
459 and normalized to the IgG condition for that replicate. (D) BMDMs were incubated with
460 unopsonized (--), IgG, or IgG+CD47 beads for 10 minutes, then lysed in LB1 lysis
461 buffer. Vav1 was immunoprecipitated, then probed for tyrosine phosphorylation.
462 Representative of $n = 2$ independent immunoprecipitations. For (B) and (C), data was
463 compared with one-way ANOVA with Holm Sidak multiple comparison test. Error bars
464 denote SEM. * denotes $p < 0.05$.

465

466 **Figure 6: Vav1 is key target of CD47-mediated inhibition of phagocytosis.** (A) TIRF
467 images show IgG (AlexaFluor 488-IgG, green) and mCherry-Vav1 (magenta) as
468 BMDMs interact with an IgG (top) or IgG+CD47 (bottom) bilayer. The linescan shows
469 the fluorescent intensity of AlexaFluor 488-IgG and mCherry-Vav1 at the indicated
470 position (white arrow in images). Intensity was normalized so that 1 is the highest

471 observed intensity and 0 is the lowest observed intensity. (B) The mean fluorescent
472 intensity of mCherry-Vav1 at IgG clusters (left) and the area of the IgG clusters (right)
473 was measured for $n=30$ cells landing on IgG or IgG+CD47 bilayers, pooled from 3
474 independent experiments. (C) Images from TIRF microscopy timelapse show IgG
475 (black) clustering as BMDMs land and spread on a bilayer with IgG (top) or IgG+CD47
476 (bottom). Graph depicts the average area of contact from $n\geq 16$ cells pooled from 3
477 separate experiments. (D) The Pearson's Correlation Coefficient was calculated for
478 mCherry-Vav1 and AlexaFluor 488-IgG in the footprint of $n\geq 38$ cells from 3 separate
479 experiments landing on IgG or IgG+CD47 bilayers. (E) BMDMs expressing membrane-
480 tethered mCherry (mCherry-CAAX) or a hyperactive Vav1 mutant (mCherry-Vav3F)
481 were incubated with unopsonized (--), IgG, or IgG+CD47 beads for 30 minutes, then
482 visualized via confocal microscopy. The average number of beads engulfed per
483 macrophage was quantified and normalized to the highest average for that experiment.
484 Points denote averages from each of the 3 replicates comprising at least 100
485 macrophages. (F) Diagram shows the proposed pathway for CD47 signaling. Data was
486 compared using an unpaired t test (B, D) or one way ANOVA with Holm Sidak multiple

487 comparison test. (E). Line and error bars denote mean and SEM. * denotes $p < 0.05$, **

488 denotes $p < 0.005$, *** denotes $p < 0.0005$. Scale bars are $10\mu\text{m}$.

489 **Supplemental figure legends**

490 **Video S1: Reaching phagocytosis of an IgG bead, related to Figure 2.**

491 Representative video of a BMDM (green) engulfing an IgG bead (magenta) via reaching
492 phagocytosis. Images are maximum projections of a confocal z-stack taken every 15
493 seconds. Scale bar is 10 μ m.

494

495 **Video S2: Sinking phagocytosis of an IgG+CD47 bead, related to Figure 2.**

496 Representative image of a BMDM (green) engulfing an IgG+CD47 bead (magenta) via
497 sinking phagocytosis. Images are maximum projections of a confocal z-stack taken
498 every 15 seconds. Scale bar is 10 μ m.

499

500 **Video S3: Failed reaching phagocytosis of IgG+CD47 bead, related to Figure 2.**

501 Representative image of a BMDM (green) attempting to engulf an IgG+CD47 bead
502 (magenta) via reaching phagocytosis. Images are maximum projections of a confocal z-
503 stack taken every 15 seconds. Scale bar is 10 μ m.

504

505 **Video S4: $Rac2^{E62K/+}$ macrophage phagocytoses a wild type L1210 cell, related to**

506 **Figure 4.**

507 Representative video of a BMDM (green) phagocytosing a L1210 cell (CellTrace Far
508 Red; magenta). Images were taken every 3 minutes. Scale bar is 10 μ m.

509

510 **Supplementary Figure 1: Validation of Rho GTPase inhibitors, related to Figure 3.**

511 To validate that the GTPase inhibitors used in Figure 3 had the expected effects on

512 macrophage actin dynamics, BMDMs were incubated for 24 hours in DMEM
513 (untreated), or DMEM supplemented with 1mM NSC23766, 500nM MBQ-167, or
514 0.5µg/mL C3 transferase, then fixed and stained with GFP-conjugated phalloidin.
515 NSC23766 and MBQ-167 had similar effects on macrophage morphology, as both
516 induced cell rounding, shrinkage, and reduction of lamellipodia and cell polarity,
517 characteristic of Rac inhibition. On the other hand, C3 transferase induced loss of stress
518 fibers, protrusion of dendritic extensions and collapse of the cell body, as expected with
519 RhoA inhibition. Scale bars are 20µm.

520

521 **Supplementary Figure 2: Validation of CD47 knockout cell line, related to Figure 3**

522 To validate knockout of CD47 in L1210s, WT and CD47^{KO} L1210s were stained with
523 APC-conjugated anti-CD47 and isotype control antibodies. To the left, histograms with
524 APC signal are shown. To the right, mean fluorescent intensity of APC signal in the
525 stained populations is graphed.

526

527 **Supplementary Figure 3: Uncropped Western blots, related to Figure 5: (A)**

528 Uncropped Syk and phospho-Syk blots used in Figure 5A. (B) Uncropped total Vav and
529 phospho-Vav blots used in Figure 5A. (C) To validate efficacy of Vav
530 immunoprecipitation, the following samples were collected, run on an SDS-PAGE gel
531 and probed for total Vav: whole cell emulsion, cell pellet, cell lysate (input used for IP),
532 flow through, first wash, and elution (containing immunoprecipitated Vav). To the right,
533 uncropped blots used in Figure 5D are shown.

534

535 **Supplementary Figure 4: Vav3F has morphological effects consistent with Vav1**
536 **activation, related to Figure 6**

537 Two representative BMDMs expressing Vav3F show distinct morphology, characteristic
538 of Vav1 hyperactivation. Vav3F-expressing cells are more spread and have increased
539 lamellipodia and ruffles, as shown previously⁷⁸. Vav3F-expressing cells also have large
540 numbers of macropinosomes, as expected with increased Vav-dependent
541 macropinocytosis. Scale bars are 20 μ m.

542 **Methods**

543 **Key Resources Table**

544 **Resource Availability**

545 Lead Contact

546 Further information and requests for reagents and resources should be directed to and
547 will be fulfilled by the Lead Contact, Meghan Morrissey (morrissey@ucsb.edu)

548 Materials Availability

549 Plasmids generated in this study have been deposited to Addgene or can be obtained
550 from Lead Contact.

551 Data and Code Availability

552 Complete imaging datasets are available from the lead contact upon request. Any
553 additional information required to reanalyze the data reported in this paper is also
554 available from the lead contact upon request.

555 **Experimental Model and Study Participant Details**

556 Cell lines

557 L1210 cells were obtained from the UCSF cell culture facility and certified mycoplasma
558 and pathogen free (IMPACT III test, IDEXX BioAnalytics). The cells were cultured in
559 DMEM (GIBCO, Catalog #11965-092) supplemented with 1% Pen-Strep-Glutamine

560 (Corning, Catalog #30-009 CI) and 10% heat-inactivated fetal bovine serum (Atlanta
561 Biologicals, Catalog #S11150H) at 37°C. Lenti-X 293T cells (Takara Biosciences, Cat#
562 632180) were cultured in DMEM, 10% FBS, 1% PSG media at 37°C.

563 Bone-marrow derived macrophage cell culture

564 Six- to ten-week old male and female C57BL/6 mice were sacrificed by CO₂ inhalation.
565 Hips and femurs were dissected and bone marrow was harvested as previously
566 described⁹⁷. Macrophage progenitors were differentiated for seven days in RPMI-1640
567 (GIBCO, Catalog # 72400120) supplemented with 10% heat-inactivated fetal bovine
568 serum, 1% Pen-Strep-Glutamine, and 20% L929-conditioned media. Macrophage
569 differentiation was confirmed by flow cytometry identifying CD11b and F4/80 double
570 positive cells. Differentiated BMDMs were used for experiments from days 7 to 11.

571 **Method Details**

572 Lentivirus production and infection

573 All constructs were expressed in either BMDMs or L1210s using lentiviral infection.
574 Lentivirus was produced in Lenti-X 293T cells transfected with pMD2.g (gift from Didier
575 Trono, Addgene plasmid #12259 containing VSV-G envelope protein), pCMV-dR8.2 (gift
576 from Bob Weinberg, Addgene plasmid #8455)⁹⁸, and a lentiviral backbone containing
577 the construct of interest using lipofectamine LTX (Invitrogen, Cat #15338-100). The
578 media was harvested 72 h post-transfection, filtered through a 0.45 µm filter (Millipore,
579 Cat# SLHVM33RS) and concentrated using LentiX (Takara Biosciences, Cat# 631232).

580 For BMDMs, concentrated lentivirus was added to cells on day 4 of differentiation, and
581 cells were analyzed between days 7-11.

582 Supported lipid bilayer assembly

583 SUV preparation

584 For beads, the following chloroform-suspended lipids were mixed and desiccated
585 overnight to remove chloroform: 95.3% POPC (Avanti, Cat# 850457), 2.5% biotinyl cap
586 PE (Avanti, Cat# 870273), 2% DGS-NTA (Avanti, Cat# 790404), 0.1% PEG5000-PE
587 (Avanti, Cat# 880230), and either 0.1% atto390-DOPE (ATTO-TEC GmbH, Cat# AD
588 390-161) or 0.1% atto647-DOPE (ATTO-TEC GmbH, Cat# AD 647-151). For planar
589 bilayers, the following chloroform-suspended lipids were mixed and desiccated
590 overnight to remove chloroform: 97.8% POPC (Avanti, Cat# 850457), 1% biotinyl cap
591 PE (Avanti, Cat# 870273), 1% DGS-NTA (Avanti, Cat# 790404), 0.1% PEG5000-PE
592 (Avanti, Cat# 880230), and 0.1% atto647-DOPE (ATTO-TEC GmbH, Cat# AD 647-
593 151). The lipid sheets were resuspended in PBS, pH7.2 (GIBCO, Cat# 20012050) at
594 10mM concentration and stored under inert nitrogen gas. The lipids were broken into
595 small unilamellar vesicles via several rounds of freeze-thaws. The lipids were then
596 stored at -80°C under nitrogen. To remove aggregated lipids, the solution was diluted to
597 2 mM and filtered through a 0.22 µm filter (Millipore, Cat# SLLG013SL) immediately
598 prior to use.

599 Planar bilayer preparation for TIRF microscopy

600 Ibidi coverslips (Cat# 10812) were piranha cleaned. Supported lipid bilayers were
601 assembled in custom PDMS (Dow Corning, cat# 3097366-0516 and 3097358-1004)
602 chambers at room temperature for 1 h. Assembled bilayers were washed 6x with PBS,
603 then blocked with 0.2% casein (Sigma, cat# C5890) in PBS for 15 minutes. Anti-biotin
604 IgG (Jackson ImmunoResearch Laboratories Cat# 200-002-211) was added at 1 nM,
605 and 10x-His tagged CD47 (Sino Biological, Cat# 57231-M49H-B) was added at 10 nM.
606 Proteins were coupled to the bilayer for 45 min. Bilayers were then washed 4x with
607 0.2% casein in PBS, then 2x with serum-free RPMI at RT. Imaging was conducted in
608 serum-free RPMI at RT. Bilayers were assessed for mobility by either photobleaching or
609 monitoring the mobility of single particles.

610 Bead preparation

611 Silica beads with a 5.01 μm diameter (9.79% solids, Bangs Laboratories, Cat#
612 SS05003, Lot #16595) were washed several times with PBS, mixed with 1mM SUVs in
613 PBS and incubated at room temperature for 30 min - 2 hrs with end-over-end mixing to
614 allow for bilayer formation. Beads were then washed with PBS to remove excess SUVs
615 and incubated in 0.2% casein (Sigma, Cat# C5890) in PBS for 15 min before protein
616 coupling. Anti-biotin IgG (Jackson ImmunoResearch Laboratories Cat# 200-002-211)
617 was added at 1 nM, and 10x-His tagged CD47 (Sino Biological, Cat# 57231-M49H-B)
618 was added at 10 nM. We estimated the amount of IgG coupling to the beads by
619 comparing the fluorescence of AlexaFluor-647 IgG to calibrated fluorescent beads
620 (Quantum AlexaFluor647, Bangs Lab) and measured 200-360 molecules/ μm^2 ⁹⁹. The
621 CD47 density was selected to give a consistent, strong suppression of phagocytosis.

622 Proteins were coupled to the bilayer for 30 min at room temperature with end-over-end
623 mixing.

624 Phagocytosis assays

625 Bead engulfment

626 50,000 BMDMs were plated per well in a 96-well glass bottom MatriPlate (Brooks, Cat#
627 MGB096-1-2-LG-L) between 24-48 h prior to the experiment. $\sim 8 \times 10^5$ beads were
628 added to wells and engulfment was allowed to proceed for 30 min. The cells were
629 imaged using spinning disc microscopy (40 × 0.95 NA Plan Apo air). Internalized
630 particles were identified by their fluorescent supported lipid bilayer, and counted in
631 ImageJ by a blinded analyzer using Blind-Analysis-Tools-1.0 ImageJ plug in⁶¹. For each
632 well, at least 100 macrophages were scored. When Rho GTPase inhibitors were used,
633 BMDMs plated 24 h earlier were incubated with either 1mM NSC23766 (APExBIO, Cat#
634 A1952), 500nM MBQ-167 (MedChemExpress, Cat# HY-112842), or 0.5ug/mL C3
635 Transferase (Cytoskeleton, Cat# CT04-A) for 24 hours before beads were added to
636 cells.

637 L1210 engulfment

638 40,000 WT or Rac2^{+E62K} BMDMs were plated per well in a 96-well glass bottom plate
639 24-48 hours prior to the experiment. WT or CD47^{KO} L1210 cells were dyed with
640 CellTrace Far Red (Thermo, Cat# C34572), incubated with an anti-mouse CD20
641 antibody (Genentech, clone 5D2) at 5ug/mL, then added to wells at 80,000 cells per
642 well and imaged every 3 min for 10 hours. For each well, at least 100 macrophages

643 were scored by a blind analyzer. Phagocytic macrophages were characterized as
644 BMDMs that engulfed 1 or more whole, viable L1210 cell targets. When Rho GTPase
645 inhibitors were used, BMDMs plated 24 h earlier were incubated with either 1mM
646 NSC23766 (APExBIO, Cat# A1952), 500nM MBQ-167 (MedChemExpress, Cat# HY-
647 112842), or 0.5ug/mL C3 Transferase (Cytoskeleton, Cat# CT04-A) for 24 hours.
648 Inhibitors were then washed out before adding L1210 cells.

649 Kinetics of engulfment

650 GFP-CAAX expressing BMDMs were plated as described in the bead engulfment assay
651 24-48 hours prior to the experiment. Using ND acquisition in Elements, 2-3 positions per
652 well were manually selected. Approximately 4×10^5 beads were added and
653 phagocytosis was imaged at 15 s intervals with 1um z-steps for 30 min. Bead binding
654 was determined by counting the number of beads that came into and remained in
655 contact with the cells throughout the imaging time, and is shown as a percentage of
656 total beads. Initiation was identified by the frame in which the process of bead
657 internalization began, indicated by membrane deforming or extending around the bead.
658 Engulfment completion was identified by complete internalization of the bead by the
659 macrophage. The initiation time was quantified as the amount of time between bead
660 contact (the first frame in which the bead contacted the macrophage) and engulfment
661 initiation (the first frame in which bead internalization was visualized) and was only
662 measured for beads that were completely internalized by the end of the imaging time.
663 The engulfment time was quantified as the amount of time between engulfment initiation
664 and engulfment completion (the first frame in which the bead has been fully internalized
665 by the cell). In Fig. 2C, an engulfment event was classified as reaching phagocytosis if

666 the target was engulfed via membrane protrusions that extended away from the cell
667 body of the macrophage, out around the target. Alternatively, an engulfment event was
668 classified as sinking phagocytosis if the target was slowly pulled into the cell, in the
669 absence of any such membrane protrusions. Analysis was blinded using Blind-Analysis-
670 Tools-1.0 ImageJ plug in⁶¹.

671 TIRF imaging

672 After assembling bilayers in TIRF chambers as described earlier, BMDMs were
673 removed from their culture dish using 5% EDTA in PBS and resuspended in serum-free
674 RPMI before being added to the TIRF chamber for imaging.

675 Quantification of IgG clusters and Vav1 recruitment

676 After 15 min of interacting with the bilayer, cells that had spread on the bilayer surface
677 were selected for analysis. Otsu thresholding in ImageJ was used to select IgG clusters
678 in an unbiased manner. This selection was used to generate an ROI that was then
679 applied to the Vav-mCherry channel. The area of the ROI (area of IgG clusters) and the
680 mean Vav1 intensity within that ROI were measured.

681 Pearson's Correlation Coefficient

682 The region of cell-bilayer contact was manually selected in ImageJ and the Pearson's
683 correlation coefficient between AlexaFluor488-IgG and Vav-mCherry was measured
684 using the JaCoP plugin¹⁰⁰.

685 Quantification of cell-bilayer contact area

686 For 6C the area of the cell contacting the bilayer was traced in ImageJ beginning with
687 the first frame where the cell can be detected. Only cells with mobile IgG clusters were
688 included.

689 Measuring actin recruitment to cup rims

690 50,000 BMDMs were plated per well in a 96-well glass bottom MatriPlate between 24-
691 48 h prior to the experiment. $\sim 8 \times 10^5$ beads were added to wells and engulfment was
692 allowed to proceed for 15 minutes. Cells were then fixed with 4% PFA for 10 minutes,
693 permeabilized with 0.1% Triton-X, and stained with 14nM acti-stain 488 phalloidin
694 (Cytoskeleton, Cat# PHDG1). Cups that were between 50-100% complete were
695 analyzed.

696 Generation and validation of CD47^{KO} L1210 cell line

697 To generate stable L1210 CD47^{KO} lines, WT L1210s were infected with a 3rd
698 generation lentiviral backbone encoding Cas9¹⁰¹ and sgRNAs (sequence:
699 GATAAGCGCGATGCCATGG) targeting the 2nd exon of mouse CD47. Single cells
700 expressing Cas9 and guide RNAs were sorted for monoclonal populations. To validate
701 knockout of CD47, surface expression of CD47 was assessed via FACS (Fig. S1).
702 Single-cell sorted monoclonal populations, as well as WT L1210s, were washed 2x with
703 FACS blocking buffer (PBS, 0.5% BSA, 2mM EDTA), incubated in blocking buffer on ice
704 for 10 minutes, then incubated with an APC-conjugated anti-CD47 antibody (BioLegend,
705 cat# 127514) or an APC-conjugated isotype control antibody (BioLegend, cat# 400511)

706 at 10 ug/mL for 30 minutes on ice in the dark. Cells were then washed 2x with blocking
707 buffer and analyzed using an Attune NxT (Invitrogen).

708 Immunoblotting

709 $\sim 1.6 \times 10^7$ beads were added to 1 million BMDMs in one well of a 6-well plate, then 10
710 minutes later cells were washed with PBS and lysed directly in culture plates with 100ul
711 2X Laemmli sample buffer containing 2-mercaptoethanol. Cells were scraped and
712 collected, then boiled for 3 minutes at 95°C and sonicated for 30sec at 50% amplitude
713 (Branson). Proteins were resolved on 4-20% SDS-PAGE gels (Bio-Rad #4561095)
714 before being transferred to 0.45 μ m LF PVDF membranes using a wet-transfer method
715 with Towbin transfer buffer (192 mM Glycine, 25 mM Tris-base, 20% methanol).
716 Membranes were blocked in 3% BSA (Fisher Scientific #BP1605-100) in TBST (0.1%
717 Tween-20) for 1 hour, then probed with desired primary antibody in 3% BSA in TBST
718 overnight at 4°C with gentle agitation. The following day, membranes were washed 3x5
719 minutes with TBST before probing with species-specific HRP-conjugated secondary
720 antibodies (Bio-Rad, Cat# 1706515) dissolved in 3% BSA in TBST for 1 hour.
721 Membranes were then washed 3x5 minutes with TBST, followed by one wash with TBS
722 before visualization of chemiluminescence using either Pierce ECL2 Western Blotting
723 Substrate (Thermo Scientific #PI80196) or Pierce SuperSignal West Femto Substrate
724 (Thermo Scientific #34095) on a ChemiDoc MP imaging system (Bio-Rad). The
725 antibodies used for immunoblotting in this study are as follows: anti-Vav1 (CST,
726 Cat#2502S), anti-phosphoVav1 (Abcam, Cat#ab76225), anti-Syk (CST, Cat#13198),
727 anti-phosphoSyk (CST, Cat#2717), anti-phosphoTyrosine (CST, Cat#8954).

728 Immunoprecipitation

729 $\sim 8 \times 10^7$ beads were added to 10-15 million BMDMs in a 10cm plate, then 10 minutes
730 later cells were washed with PBS and lysed with buffer LB1 (50 mM HEPES pH 7.6,
731 100 mM NaCl, 50 mM KCl, 10 mM MgCl₂, 0.5 % IPEGAL CA-630, 0.1% Na-
732 deoxycholate, 2 mM Na₃VO₄, and 20 mM NaF) containing 1X protease inhibitor
733 (ThermoFisher, Cat# 78430), benzonase (EMD-Millipore, Cat# 101697), and 0.5 mM
734 EDTA directly in 10cm plates. Cells were scraped and collected. Cells were incubated
735 on ice for 15 minutes, passed 5x through a 25G hypodermic needle to shear cells and
736 genomic DNA, then incubated another 15 minutes on ice with mixing by inversion. The
737 resulting lysate was then spun 15,000g x 20 minutes at 4°C and the supernatant was
738 collected. Lysate was then pre-cleared with Protein A agarose beads (Cell Signaling
739 Technology, Cat# 9863S), that were pre-washed twice in LB1, for 30 minutes at 4°C to
740 reduce non-specific binding. Beads were then spun down 5000g x 1 min and
741 supernatant collected. 0.7 ug of Vav1 antibody (CST, Cat# 2502S) was added directly
742 to the lysate and incubated for 2 hours at 4°C with gentle inversion. Protein A agarose
743 slurry, that was pre-washed twice in buffer LB1, was added to each lysate + antibody
744 mix and incubated for another 2 hours at 4°C with gentle inversion. The protein A
745 agarose was then washed four times with buffer LB1 and bound proteins were eluted
746 with elution buffer (0.2 M glycine pH 2.5) by incubating for 10 minutes shaking at 1100
747 rpm at 4°C. Beads were spun 5000g x 1 min and eluates were collected. The elution
748 was performed twice and pooled together. To neutralize the pH, Tris-Cl pH 8.5 was
749 added to a final concentration of 100 mM, followed by addition of 2X Laemmli sample
750 buffer with 2-mercaptoethanol to prepare samples for SDS-PAGE.

751 Microscopy and analysis

752 Images were acquired on a spinning disc confocal microscope (Nikon Ti-Eclipse
753 inverted microscope with a Yokogawa spinning disk unit and an Orca Fusion BT scMos
754 camera) equipped with a 40 × 0.95 NA air and a 100 × 1.49 NA oil immersion objective.
755 The microscope is also equipped with a piezo Z drive and an OkoLabs stage top
756 incubator for temperature, CO₂ and humidity control. TIRF imaging was performed with
757 an iLas2 ring TIRF on the same microscope base and same camera. The microscope
758 was controlled using Nikon Elements.

759 **Quantification and Statistical Analysis**

760 Statistical analysis was performed in Prism 8 (GraphPad). The statistical test used is
761 indicated in the relevant figure legend. Sample sizes were predetermined and indicated
762 in the relevant figure legend. In general the analyzer was blinded during analysis using
763 either manual renaming of the files or the Blind-Analysis-Tools-1.0 ImageJ plug in.
764 The details of each quantification method and blinding strategy are included in the
765 Methods section.

766 **Acknowledgments**

767 We thank Melanie Rodriguez for providing Rac2^{E62K/+} femurs for BMDM isolation. We
768 also thank members of the Morrissey lab for critical feedback on the manuscript.
769 Addgene plasmid 52961 was a gift from Feng Zhang. CJS was supported by the UC
770 Santa Barbara Chancellor's Fellowship. This work was funded by NCI 1DP1CA300850

771 to DJM; NIGMS R35GM146784 to BMG; University of California Cancer Research
772 Coordinating Committee grant C23CR5592 and NIGMS R35GM146935 to MAM.

773 **Author contributions**

774 Conceptualization, W.D.M., M.A.M.; Methodology, W.D.M., A.K.M., C.J.S. M.A.M.;
775 Validation, W.D.M.; Formal Analysis W.D.M.; Investigation, W.D.M., A.K.M., C.J.S., AB;
776 Resources, W.D.M., B.M.G, D.J.M, M.A.M.; Writing–Original Draft, W.D.M., M.A.M.;
777 Writing–Review and Editing, W.D.M., B.M.G, D.J.M, M.A.M.; Visualization, W.D.M.;
778 Supervision, B.M.G, D.J.M, M.A.M.; Funding Acquisition, B.M.G, D.J.M, M.A.M.

779 **Declaration of interests**

780 The authors declare no competing interests.

781 **Supplemental Information**

782 Document S1. Figures S1-S3

783 Video S1. Reaching phagocytosis of IgG bead, related to Figure 2

784 Video S2. Sinking phagocytosis of IgG+CD47 bead, related to Figure 2

785 Video S3. Failed reaching phagocytosis, related to Figure 2

786 Video S4: Rac2^{E62K/+} macrophage phagocytoses a wild type L1210 cell, related to

787 Figure 4.

788 References

789

- 790 1. Rumpret, M. *et al.* Functional categories of immune inhibitory receptors. *Nat. Rev.*
791 *Immunol.* **20**, 771–780 (2020).
- 792 2. Daëron, M., Jaeger, S., Du Pasquier, L. & Vivier, E. Immunoreceptor tyrosine-based
793 inhibition motifs: a quest in the past and future. *Immunol. Rev.* **224**, 11–43 (2008).
- 794 3. Grebinoski, S. & Vignali, D. A. A. Inhibitory receptor agonists: The future of
795 autoimmune disease therapeutics? *Curr. Opin. Immunol.* **67**, 1–9 (2020).
- 796 4. Schnell, A., Bod, L., Madi, A. & Kuchroo, V. K. The yin and yang of co-inhibitory
797 receptors: toward anti-tumor immunity without autoimmunity. *Cell Res.* **30**, 285–299
798 (2020).
- 799 5. Freeman, S. & Grinstein, S. Promoters and Antagonists of Phagocytosis: A Plastic
800 and Tunable Response. *Annu. Rev. Cell Dev. Biol.* **37**, 89–114 (2021).
- 801 6. Veillette, A. & Chen, J. SIRP α –CD47 Immune Checkpoint Blockade in Anticancer
802 Therapy. *Trends Immunol.* **39**, 173–184 (2018).
- 803 7. Dilillo, D. J., Tan, G. S., Palese, P. & Ravetch, J. V. Broadly neutralizing
804 hemagglutinin stalk-specific antibodies require FcR interactions for protection
805 against influenza virus in vivo. *Nat. Med.* **20**, 143–151 (2014).
- 806 8. Erwig, L. P. & Gow, N. A. R. Interactions of fungal pathogens with phagocytes. *Nat.*
807 *Rev. Microbiol.* **14**, 163–176 (2016).
- 808 9. Weiskopf, K. & Weissman, I. L. Macrophages are critical effectors of antibody
809 therapies for cancer. *mAbs* **7**, 303–310 (2015).
- 810 10. Shi, Y. *et al.* Trastuzumab triggers phagocytic killing of high HER2 cancer cells in

- 811 vitro and in vivo by interaction with Fc γ receptors on macrophages. *J. Immunol.*
812 *Baltim. Md 1950* **194**, 4379–4386 (2015).
- 813 11. Chen, X., Song, X., Li, K. & Zhang, T. Fc γ R-Binding Is an Important Functional
814 Attribute for Immune Checkpoint Antibodies in Cancer Immunotherapy. *Front.*
815 *Immunol.* **10**, 292 (2019).
- 816 12. Uchida, J. *et al.* The innate mononuclear phagocyte network depletes B
817 lymphocytes through Fc receptor-dependent mechanisms during anti-CD20
818 antibody immunotherapy. *J. Exp. Med.* **199**, 1659–1669 (2004).
- 819 13. Nimmerjahn, F. & Ravetch, J. V. Fc γ receptors as regulators of immune responses.
820 *Nat. Rev. Immunol.* **8**, 34–47 (2008).
- 821 14. Jaiswal, S. *et al.* CD47 Is Upregulated on Circulating Hematopoietic Stem Cells and
822 Leukemia Cells to Avoid Phagocytosis. *Cell* **138**, 271–285 (2009).
- 823 15. Majeti, R. *et al.* CD47 Is an Adverse Prognostic Factor and Therapeutic Antibody
824 Target on Human Acute Myeloid Leukemia Stem Cells. *Cell* **138**, 286–299 (2009).
- 825 16. Oldenborg, P. A. *et al.* Role of CD47 as a marker of self on red blood cells. *Science*
826 **288**, 2051–4 (2000).
- 827 17. Okazawa, H. *et al.* Negative Regulation of Phagocytosis in Macrophages by the
828 CD47-SHPS-1 System. *J. Immunol.* **174**, 2004–2011 (2005).
- 829 18. Veillette, A., Thibaudeau, E. & Latour, S. High expression of inhibitory receptor
830 SHPS-1 and its association with protein-tyrosine phosphatase SHP-1 in
831 macrophages. *J. Biol. Chem.* **273**, 22719–22728 (1998).
- 832 19. Oldenborg, P.-A., Gresham, H. D. & Lindberg, F. P. Cd47-Signal Regulatory Protein
833 α (Sirp α) Regulates Fc γ and Complement Receptor–Mediated Phagocytosis. *J. Exp.*

- 834 *Med.* **193**, 855–862 (2001).
- 835 20. Barclay, A. N. & Van Den Berg, T. K. The Interaction Between Signal Regulatory
836 Protein Alpha (SIRP α) and CD47: Structure, Function, and Therapeutic Target.
837 *Annu. Rev. Immunol.* **32**, 25–50 (2014).
- 838 21. Jiang, P., Lagenaur, C. F. & Narayanan, V. Integrin-associated protein is a ligand for
839 the P84 neural adhesion molecule. *J. Biol. Chem.* **274**, 559–62 (1999).
- 840 22. Tal, M. C. *et al.* P66 is a bacterial mimic of CD47 that binds the anti-phagocytic
841 receptor SIRP α and facilitates macrophage evasion by *Borrelia burgdorferi*.
842 2024.04.29.591704 Preprint at <https://doi.org/10.1101/2024.04.29.591704> (2024).
- 843 23. Angabo, S. *et al.* CD47 and thrombospondin-1 contribute to immune evasion by
844 *Porphyromonas gingivalis*. *Proc. Natl. Acad. Sci.* **121**, e2405534121 (2024).
- 845 24. Sonnert, N. D. *et al.* A host–microbiota interactome reveals extensive transkingdom
846 connectivity. *Nature* **628**, 171–179 (2024).
- 847 25. Willingham, S. B. *et al.* The CD47-signal regulatory protein alpha (SIRP α) interaction
848 is a therapeutic target for human solid tumors. *Proc. Natl. Acad. Sci.* **109**, 6662–
849 6667 (2012).
- 850 26. Ansell, S. M. *et al.* Phase 1 Study of the CD47 Blocker TTI-621 in Patients with
851 Relapsed or Refractory Hematologic Malignancies. *Clin. Cancer Res.*
852 clincanres.3706.2020 (2021) doi:10.1158/1078-0432.CCR-20-3706.
- 853 27. Advani, R. *et al.* CD47 Blockade by Hu5F9-G4 and Rituximab in Non-Hodgkin’s
854 Lymphoma. *N. Engl. J. Med.* **379**, 1711–1721 (2018).
- 855 28. Lakhani, N. J. *et al.* Evorpcept alone and in combination with pembrolizumab or
856 trastuzumab in patients with advanced solid tumours (ASPEN-01): a first-in-human,

- 857 open-label, multicentre, phase 1 dose-escalation and dose-expansion study. *Lancet*
858 *Oncol.* **22**, 1740–1751 (2021).
- 859 29. Johnson, L. D. S. *et al.* Targeting CD47 in Sézary syndrome with SIRPαFc. *Blood*
860 *Adv.* **3**, 1145–1153 (2019).
- 861 30. Sikic, B. I. *et al.* First-in-Human, First-in-Class Phase I Trial of the Anti-CD47
862 Antibody Hu5F9-G4 in Patients With Advanced Cancers. *J. Clin. Oncol. Off. J. Am.*
863 *Soc. Clin. Oncol.* **37**, 946–953 (2019).
- 864 31. Tseng, D. *et al.* Anti-CD47 antibody-mediated phagocytosis of cancer by
865 macrophages primes an effective antitumor T-cell response. *Proc. Natl. Acad. Sci.*
866 **110**, 11103–11108 (2013).
- 867 32. Liu, X. *et al.* CD47 blockade triggers T cell–mediated destruction of immunogenic
868 tumors. *Nat. Med.* **21**, 1209–1215 (2015).
- 869 33. Kojima, Y. *et al.* CD47-blocking antibodies restore phagocytosis and prevent
870 atherosclerosis. *Nature* **536**, 86–90 (2016).
- 871 34. Cham, L. B. *et al.* Immunotherapeutic Blockade of CD47 Inhibitory Signaling
872 Enhances Innate and Adaptive Immune Responses to Viral Infection. *CellReports*
873 **31**, 107494 (2020).
- 874 35. Rodriguez, P. L. *et al.* Minimal ‘Self’ Peptides That Inhibit Phagocytic Clearance and
875 Enhance Delivery of Nanoparticles. *Science* **339**, 971–975 (2013).
- 876 36. Yamada-Hunter, S. A. *et al.* Engineered CD47 protects T cells for enhanced
877 antitumour immunity. *Nature* **630**, 457–465 (2024).
- 878 37. Stachelek, S. J. *et al.* The effect of CD47 modified polymer surfaces on
879 inflammatory cell attachment and activation. *Biomaterials* **32**, 4317–4326 (2011).

- 880 38. Sosale, N. G. *et al.* “Marker of Self” CD47 on lentiviral vectors decreases
881 macrophage-mediated clearance and increases delivery to SIRPA-expressing lung
882 carcinoma tumors. *Mol. Ther. - Methods Clin. Dev.* **3**, 16080 (2016).
- 883 39. Sakano, Y. *et al.* SIRP α engagement regulates ILC2 effector function and alleviates
884 airway hyperreactivity via modulating energy metabolism. *Cell. Mol. Immunol.* **21**,
885 1158–1174 (2024).
- 886 40. Xie, M. M. *et al.* An agonistic anti-signal regulatory protein α antibody for chronic
887 inflammatory diseases. *Cell Rep. Med.* **4**, 101130 (2023).
- 888 41. Kharitononkov, A. *et al.* A family of proteins that inhibit signalling through tyrosine
889 kinase receptors. *Nature* **386**, 181–186 (1997).
- 890 42. Morrissey, M. A., Kern, N. & Vale, R. D. CD47 ligation repositions the inhibitory
891 receptor SIRPA to suppress integrin activation and phagocytosis. *Immunity* **ePub**
892 **Aug 7**, 290-302.e6 (2020).
- 893 43. Fujioka, Y. *et al.* A novel membrane glycoprotein, SHPS-1, that binds the SH2-
894 domain-containing protein tyrosine phosphatase SHP-2 in response to mitogens and
895 cell adhesion. *Mol. Cell. Biol.* **16**, 6887–99 (1996).
- 896 44. Noguchi, T. *et al.* Characterization of a 115-kDa protein that binds to SH-PTP2, a
897 protein-tyrosine phosphatase with Src homology 2 domains, in Chinese hamster
898 ovary cells. *J. Biol. Chem.* **271**, 27652–8 (1996).
- 899 45. Myers, D. R. *et al.* Shp1 Loss Enhances Macrophage Effector Function and
900 Promotes Anti-Tumor Immunity. *Front. Immunol.* **11**, (2020).
- 901 46. Tsai, R. K. & Discher, D. E. Inhibition of ‘self’ engulfment through deactivation of
902 myosin-II at the phagocytic synapse between human cells. *J. Cell Biol.* **180**, 989–

- 903 1003 (2008).
- 904 47. Joffe, A. M., Bakalar, M. H. & Fletcher, D. A. Macrophage phagocytosis assay with
905 reconstituted target particles. *Nat. Protoc.* 2020 157 **15**, 2230–2246 (2020).
- 906 48. Suter, E. C. *et al.* Antibody:CD47 ratio regulates macrophage phagocytosis through
907 competitive receptor phosphorylation. *Cell Rep.* **36**, (2021).
- 908 49. Kaplan, G. Differences in the Mode of Phagocytosis with Fc and C3 Receptors in
909 Macrophages. *Scand. J. Immunol.* **6**, 797–807 (1977).
- 910 50. Munthe-Kaas, A. C., Kaplan, G. & Seljelid, R. On the mechanism of internalization of
911 opsonized particles by rat Kupffer cells in vitro. *Exp. Cell Res.* **103**, 201–212 (1976).
- 912 51. Underhill, D. M. & Goodridge, H. S. Information processing during phagocytosis.
913 *Nat. Rev. Immunol.* **12**, 492–502 (2012).
- 914 52. Caron, E. & Hall, A. Identification of Two Distinct Mechanisms of Phagocytosis
915 Controlled by Different Rho GTPases. *Science* **282**, 1717–1721 (1998).
- 916 53. Walbaum, S. *et al.* Complement receptor 3 mediates both sinking phagocytosis and
917 phagocytic cup formation *via* distinct mechanisms. *J. Biol. Chem.* **296**, 100256
918 (2021).
- 919 54. Jaumouillé, V., Cartagena-Rivera, A. X. & Waterman, C. M. Coupling of β 2 integrins
920 to actin by a mechanosensitive molecular clutch drives complement receptor-
921 mediated phagocytosis. *Nat. Cell Biol.* **21**, 1357–1369 (2019).
- 922 55. Vorselen, D. *et al.* Cell surface receptors TREM2, CD14 and integrin α M β 2 drive
923 sinking engulfment in phosphatidylserine-mediated phagocytosis.
924 2022.07.30.502145 Preprint at <https://doi.org/10.1101/2022.07.30.502145> (2022).
- 925 56. Hsu, A. P. *et al.* Dominant activating RAC2 mutation with lymphopenia,

- 926 immunodeficiency, and cytoskeletal defects. *Blood* **133**, 1977–1988 (2019).
- 927 57. Mishra, A. K. *et al.* Hyperactive Rac stimulates cannibalism of living target cells and
928 enhances CAR-M-mediated cancer cell killing. *Proc. Natl. Acad. Sci. U. S. A.* **120**,
929 e2310221120 (2023).
- 930 58. Goodridge, H. S., Underhill, D. M. & Touret, N. Mechanisms of Fc Receptor and
931 Dectin-1 Activation for Phagocytosis. *Traffic* **13**, 1062–1071 (2012).
- 932 59. Lin, J. *et al.* TIRF imaging of Fc gamma receptor microclusters dynamics and
933 signaling on macrophages during frustrated phagocytosis. *BMC Immunol.* **17**, 5
934 (2016).
- 935 60. Sobota, A. *et al.* Binding of IgG-Opsonized Particles to FcγR Is an Active Stage of
936 Phagocytosis That Involves Receptor Clustering and Phosphorylation. *J. Immunol.*
937 **175**, 4450–4457 (2005).
- 938 61. Kern, N., Dong, R., Douglas, S. M., Vale, R. D. & Morrissey, M. A. Tight nanoscale
939 clustering of Fcγ receptors using DNA origami promotes phagocytosis. *eLife* **10**,
940 e68311 (2021).
- 941 62. Hall, A. B. *et al.* Requirements for Vav Guanine Nucleotide Exchange Factors and
942 Rho GTPases in FcγR- and Complement-Mediated Phagocytosis. *Immunity* **24**,
943 305–316 (2006).
- 944 63. Kiener, P. A. *et al.* Cross-linking of Fc gamma receptor I (Fc gamma RI) and
945 receptor II (Fc gamma RII) on monocytic cells activates a signal transduction
946 pathway common to both Fc receptors that involves the stimulation of p72 Syk
947 protein tyrosine kinase. *J. Biol. Chem.* **268**, 24442–24448 (1993).
- 948 64. Patel, J. C., Hall, A. & Caron, E. Vav Regulates Activation of Rac but Not Cdc42

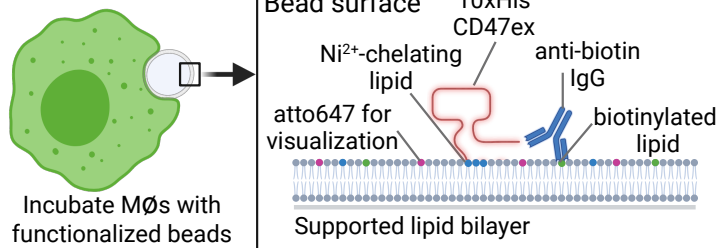
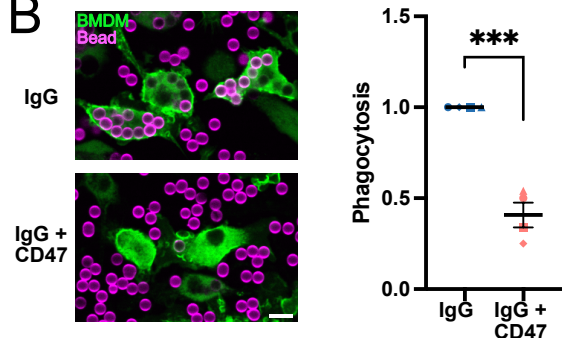
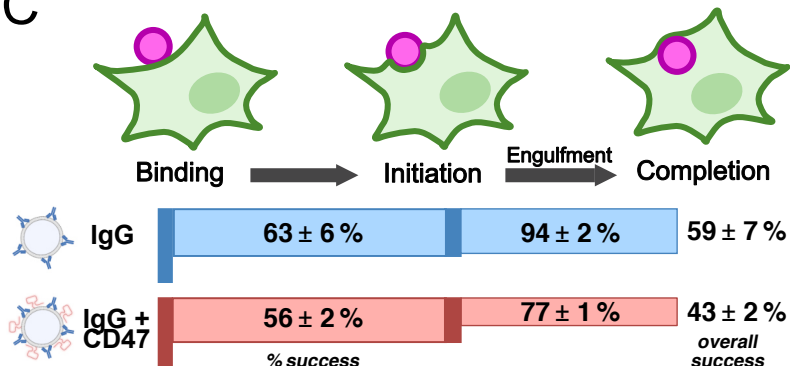
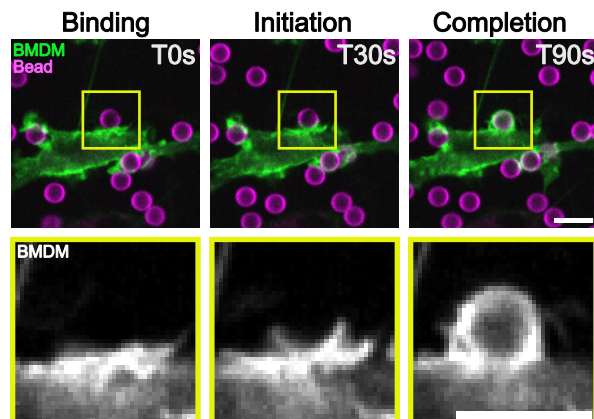
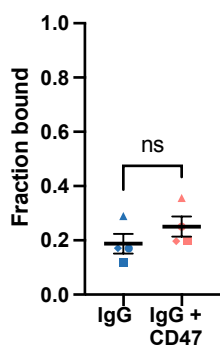
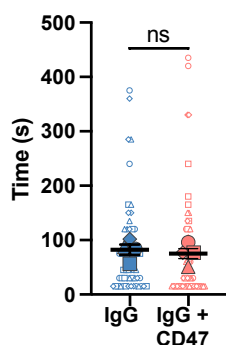
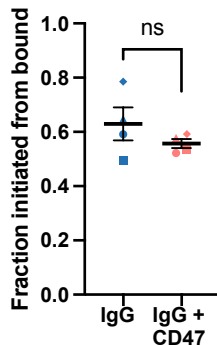
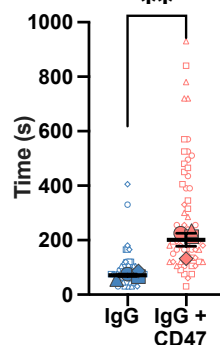
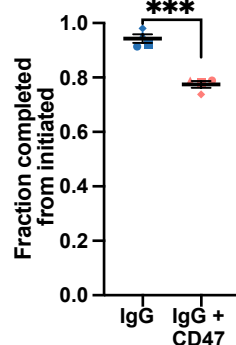
- 949 during FcγR-mediated Phagocytosis. *Mol. Biol. Cell* **13**, 1215–1226 (2002).
- 950 65. Deckert, M., Tartare-Deckert, S., Couture, C., Mustelin, T. & Altman, A. Functional
951 and Physical Interactions of Syk Family Kinases with the Vav Proto-Oncogene
952 Product. *Immunity* **5**, 591–604 (1996).
- 953 66. Mesecke, S., Urlaub, D., Busch, H., Eils, R. & Watzl, C. Integration of Activating and
954 Inhibitory Receptor Signaling by Regulated Phosphorylation of Vav1 in Immune
955 Cells. *Sci. Signal.* **4**, ra36–ra36 (2011).
- 956 67. Stebbins, C. C. *et al.* Vav1 Dephosphorylation by the Tyrosine Phosphatase SHP-1
957 as a Mechanism for Inhibition of Cellular Cytotoxicity. *Mol. Cell. Biol.* **23**, 6291–6299
958 (2003).
- 959 68. Yang, J. *et al.* Structural Basis for Substrate Specificity of Protein-tyrosine
960 Phosphatase SHP-1*. *J. Biol. Chem.* **275**, 4066–4071 (2000).
- 961 69. Wang, P., Fu, H., Snavley, D. F., Freitas, M. A. & Pei, D. Screening Combinatorial
962 Libraries by Mass Spectrometry. 2. Identification of Optimal Substrates of Protein
963 Tyrosine Phosphatase SHP-1. *Biochemistry* **41**, 6202–6210 (2002).
- 964 70. Li, Y., Hermanson, D. L., Moriarity, B. S. & Kaufman, D. S. Human iPSC-Derived
965 Natural Killer Cells Engineered with Chimeric Antigen Receptors Enhance Anti-
966 tumor Activity. *Cell Stem Cell* **23**, 181-192.e5 (2018).
- 967 71. Abate, F. *et al.* Activating mutations and translocations in the guanine exchange
968 factor VAV1 in peripheral T-cell lymphomas. *Proc. Natl. Acad. Sci.* **114**, 764–769
969 (2017).
- 970 72. Bustelo, X. R. Vav family exchange factors: an integrated regulatory and functional
971 view. *Small GTPases* **5**, e973757 (2014).

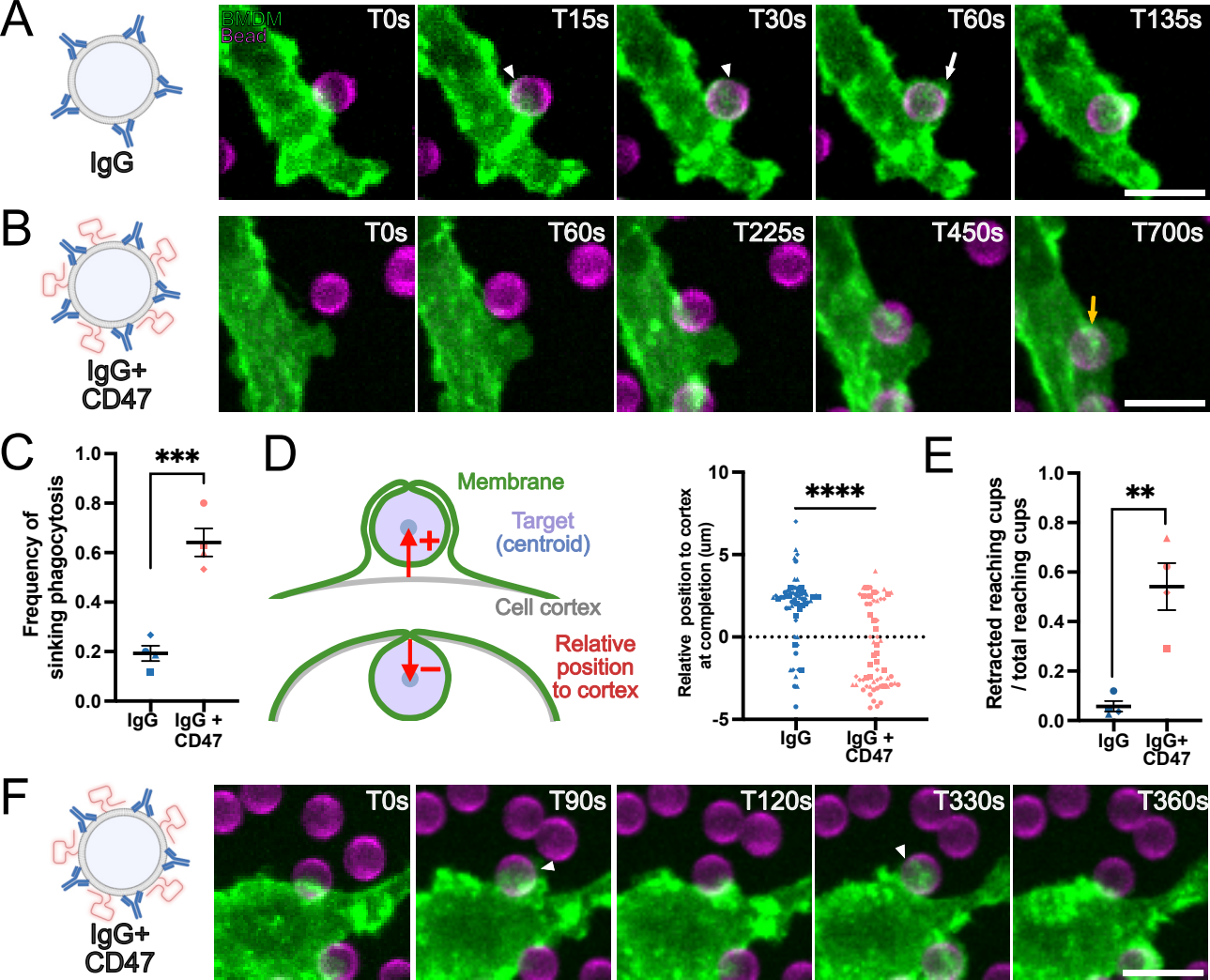
- 972 73. Hoppe, A. D. & Swanson, J. A. Cdc42, Rac1, and Rac2 Display Distinct Patterns of
973 Activation during Phagocytosis. *Mol. Biol. Cell* **15**, 3509–3519 (2004).
- 974 74. Masters, T. A., Pontes, B., Viasnoff, V., Li, Y. & Gauthier, N. C. Plasma membrane
975 tension orchestrates membrane trafficking, cytoskeletal remodeling, and
976 biochemical signaling during phagocytosis. *Proc. Natl. Acad. Sci.* **110**, 11875–11880
977 (2013).
- 978 75. Hornstein, I., Alcover, A. & Katzav, S. Vav proteins, masters of the world of
979 cytoskeleton organization. *Cell. Signal.* **16**, 1–11 (2004).
- 980 76. Aghazadeh, B., Lowry, W. E., Huang, X.-Y. & Rosen, M. K. Structural Basis for
981 Relief of Autoinhibition of the Dbl Homology Domain of Proto-Oncogene Vav by
982 Tyrosine Phosphorylation. *Cell* **102**, 625–633 (2000).
- 983 77. López-Lago, M., Lee, H., Cruz, C., Movilla, N. & Bustelo, X. R. Tyrosine
984 Phosphorylation Mediates Both Activation and Downmodulation of the Biological
985 Activity of Vav. *Mol. Cell. Biol.* **20**, 1678–1691 (2000).
- 986 78. Wilsbacher, J. L., Moores, S. L. & Brugge, J. S. An active form of Vav1 induces
987 migration of mammary epithelial cells by stimulating secretion of an epidermal
988 growth factor receptor ligand. *Cell Commun. Signal.* **4**, 5 (2006).
- 989 79. Koncz, G., Kerekes, K., Chakrabandhu, K. & Hueber, A.-O. Regulating Vav1
990 phosphorylation by the SHP-1 tyrosine phosphatase is a fine-tuning mechanism for
991 the negative regulation of DISC formation and Fas-mediated cell death signaling.
992 *Cell Death Differ.* **15**, 494–503 (2008).
- 993 80. Li, X. *et al.* The β -glucan receptor Dectin-1 activates the integrin Mac-1 in
994 neutrophils via Vav protein signaling to promote *Candida albicans* clearance. *Cell*

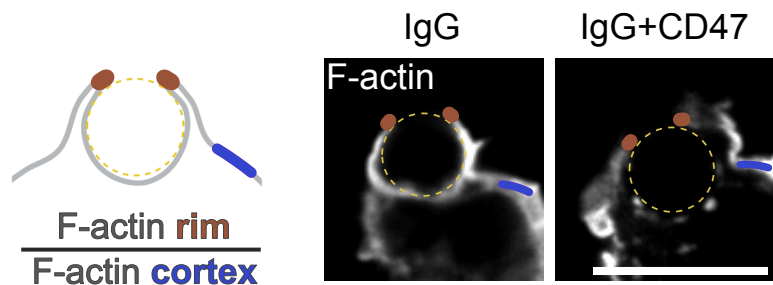
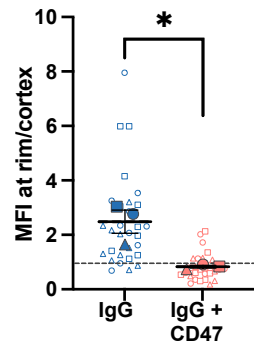
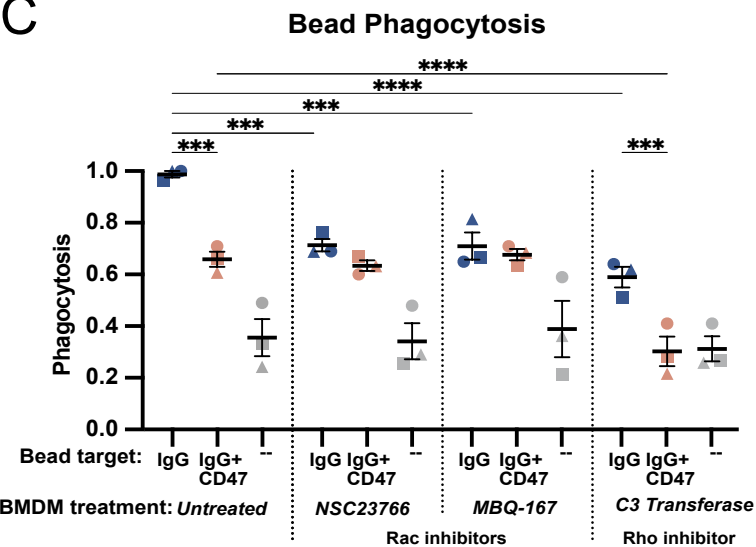
- 995 *Host Microbe* **10**, 603–615 (2011).
- 996 81. Gakidis, M. A. M. *et al.* Vav GEFs are required for β 2 integrin-dependent functions
997 of neutrophils. *J. Cell Biol.* **166**, 273–282 (2004).
- 998 82. Fischer, K.-D. *et al.* Vav is a regulator of cytoskeletal reorganization mediated by the
999 T-cell receptor. *Curr. Biol.* **8**, 554-S3 (1998).
- 1000 83. Ardouin, L. *et al.* Vav1 transduces TCR signals required for LFA-1 function and cell
1001 polarization at the immunological synapse. *Eur. J. Immunol.* **33**, 790–797 (2003).
- 1002 84. García-Bernal, D. *et al.* Vav1 and Rac Control Chemokine-promoted T Lymphocyte
1003 Adhesion Mediated by the Integrin α 4 β 1. *Mol. Biol. Cell* **16**, 3223–3235 (2005).
- 1004 85. Krawczyk, C. *et al.* Vav1 Controls Integrin Clustering and MHC/Peptide-Specific Cell
1005 Adhesion to Antigen-Presenting Cells. *Immunity* **16**, 331–343 (2002).
- 1006 86. Vorselen, D. *et al.* Phagocytic ‘teeth’ and myosin-II ‘jaw’ power target constriction
1007 during phagocytosis. *eLife* **10**, e68627 (2021).
- 1008 87. van Leeuwen, F. N., van Delft, S., Kain, H. E., van der Kammen, R. A. & Collard, J.
1009 G. Rac regulates phosphorylation of the myosin-II heavy chain, actinomyosin
1010 disassembly and cell spreading. *Nat. Cell Biol.* **1**, 242–248 (1999).
- 1011 88. Yu, Y., Zhang, Z., Walpole, G. F. W. & Yu, Y. Kinetics of phagosome maturation is
1012 coupled to their intracellular motility. *Commun. Biol.* **5**, 1–14 (2022).
- 1013 89. Zhang, Z. *et al.* Propulsive cell entry diverts pathogens from immune degradation by
1014 remodeling the phagocytic synapse. *Proc. Natl. Acad. Sci.* **120**, e2306788120
1015 (2023).
- 1016 90. Yi, T. *et al.* Splenic Dendritic Cells Survey Red Blood Cells for Missing Self-CD47 to
1017 Trigger Adaptive Immune Responses. *Immunity* **43**, 764–775 (2015).

- 1018 91. Xu, M. M. *et al.* Dendritic Cells but Not Macrophages Sense Tumor Mitochondrial
1019 DNA for Cross-priming through Signal Regulatory Protein α Signaling. *Immunity* **47**,
1020 363-373.e5 (2017).
- 1021 92. Pluvinage, J. V. *et al.* CD22 blockade restores homeostatic microglial phagocytosis
1022 in ageing brains. *Nature* **568**, 187–192 (2019).
- 1023 93. Gordon, S. R. *et al.* PD-1 expression by tumor-associated macrophages inhibits
1024 phagocytosis and tumor immunity. *Nature* **545**, 495–499 (2017).
- 1025 94. Barkal, A. A. *et al.* CD24 signalling through macrophage Siglec-10 is a target for
1026 cancer immunotherapy. *Nature* **572**, 392–396 (2019).
- 1027 95. Smith, B. A. H. & Bertozzi, C. R. The clinical impact of glycobiology: targeting
1028 selectins, Siglecs and mammalian glycans. *Nat. Rev. Drug Discov.* **20**, 217–243
1029 (2021).
- 1030 96. Theruvath, J. *et al.* Anti-GD2 synergizes with CD47 blockade to mediate tumor
1031 eradication. *Nat. Med.* **28**, 333–344 (2022).
- 1032 97. Weischenfeldt, J. & Porse, B. Bone Marrow-Derived Macrophages (BMM): Isolation
1033 and Applications. *CSH Protoc.* **2008**, pdb.prot5080 (2008).
- 1034 98. Stewart, S. A. *et al.* Lentivirus-delivered stable gene silencing by RNAi in primary
1035 cells. *RNA* **9**, 493–501 (2003).
- 1036 99. Bond, A. *et al.* Prior Fc receptor activation primes macrophages for increased
1037 sensitivity to IgG via long-term and short-term mechanisms. *Dev. Cell* (2024)
1038 doi:10.1016/j.devcel.2024.07.017.
- 1039 100. Bolte, S. & Cordelières, F. P. A guided tour into subcellular colocalization
1040 analysis in light microscopy. *J. Microsc.* **224**, 213–232 (2006).

- 1041 101. Sanjana, N. E., Shalem, O. & Zhang, F. Improved vectors and genome-wide
1042 libraries for CRISPR screening. *Nat. Methods* **11**, 783 (2014).

A**B****C****D****E****Binding probability****F****Initiation time****G****Initiation probability****H****Engulfment time****I****Completion probability**



A**B****C****D**